Available online at www.sciencedirect.com
SCIENCE DIRECT®
Journal of Nuclear Materials 329–333 (2004) 993–997
journal of nuclear materials
www.elsevier.com/locate/jnucmat

Correlation between embrittlement and bubble microstructure in helium-implanted materials

N. Yamamoto [a,*], T. Chuto [a], Y. Murase [a], J. Nagakawa [a,b]

[a] National Institute for Materials Science (NIMS), 1-2-1 Sengen, Tsukuba, Ibaraki 305-0047, Japan
[b] Interdisciplinary Graduate School of Engineering Sciences, Kyushu University, 6-1 Kasuga Koen, Kasuga, Fukuoka 816-8580, Japan

Abstract

In order to obtain further knowledge on the helium embrittlement phenomenon, bubble size distributions in helium-implanted and creep-ruptured Fe–Ni–Cr materials have been analyzed from the standpoint of bubble stability. The observed mean distance of intercrystalline helium bubbles exceeding the minimum critical size was compatible with the pore spacing on intergranularly fractured surfaces. This fact strongly suggests that unstable expansion of grain boundary bubbles with super-critical sizes acted as a working mechanism of helium embrittlement. It was found from calculations estimating the helium atom number in individual bubbles that the increase of helium retention in the inside of grains would reduce helium embrittlement to some extent.

1. Introduction

Helium embrittlement befalling to first wall/blanket structural materials has been widely recognized as one of the most crucial material issues in future nuclear fusion reactors, because much larger amounts of helium should be produced in them as compared to other types of nuclear systems such as fast breeder and light water reactors. From this viewpoint, many experimental and theoretical studies have been conducted for materials of various kinds [1,2]. Through these research activities nearly over four decades, it has been found that helium bubble microstructure is an important key to detrimental helium effects on mechanical properties.

In this article, a possible scenario to describe helium embrittlement will be discussed in terms of a stable–unstable transition of helium bubbles at grain boundaries by scrutinizing bubble size distributions obtained from helium-embrittled materials for better understanding of this harmful phenomenon. The influence of intragranular helium entrapment on the embrittlement will be also examined.

2. Experimental procedures and results

Microstructural data were collected from helium-injected and creep-ruptured Fe–Ni–Cr materials listed in Table 1. They are composed of titanium modified (DIN 1.4970 and JPCA) and low carbon (AISI 316L) 316 stainless steels, and model austenitic alloys (the 82 series alloys) having a base composition of Fe–25%Ni–15%Cr with minor additions of MC and MN forming elements.

Helium was injected into creep specimens by α-particle irradiation with a cyclotron at high temperatures. Creep rupture tests were carried out in either in situ (in-beam) or post-implantation mode at the same temperature of the irradiation. Conducted experimental

* Corresponding author. Tel.: +81-29 859 2554; fax: +81-29 859 2501.
E-mail address: yamamoto.norikazu@nims.go.jp (N. Yamamoto).

0022-3115/$ - see front matter © 2004 Elsevier B.V. All rights reserved.
doi:10.1016/j.jnucmat.2004.04.070

Table 1
Material data and creep test parameters

Material[a]	Nominal composition	Test mode	Test temperature (K)	Applied stress (MPa)	He concentration (appm)	He-implantation rate (appm/s)	Ref.
DIN 1.4970 CW	15Ni15Cr–Ti–C	In-beam	873	400–470	150–1200	2×10^{-2}	[3]
AISI 316L CW	12Ni18Cr–low C	In-beam	873	240–300	170–500	3×10^{-2}	[3]
JPCA SA	16Ni15Cr–Ti–C	Post-impl.	923	185–237	50	6×10^{-4}	[4]
JPCA TMT	16Ni15Cr–Ti–C	Post-impl.	923	180–306	50	$4–9\times10^{-4}$	[4]
8201 TMT	25Ni15Cr–Ti–C	Post-impl.	923	120	50	9×10^{-4}	[5]
8202 TMT	25Ni15Cr–Zr–C	Post-impl.	923	120	50	8×10^{-4}	[5]
8203 TMT	25Ni15Cr–V–C	Post-impl.	923	120	50	1×10^{-3}	[5]
8204 TMT	25Ni15Cr–V–N,C	Post-impl.	923	120	50	8×10^{-4}	[5]
8206 TMT	25Ni15Cr–Ti,Nb–C	Post-impl.	923	120	50	9×10^{-4}	[5]
8207 TMT	25Ni15Cr–V,Ti–C	Post-impl.	923	120	50	1×10^{-3}	[5]

[a] SA: solution annealing; CW: cold work; TMT: thermomechanical treatment.

parameters except for temperature were varied over rather wide regions. Details of each experiment are given in the related reference in the last column of Table 1.

Mechanical deterioration by helium was observed for all samples tested, accompanying an increasing trend of intercrystalline failure. Fig. 1 reveals a representative feature of intergranular decohesion induced by helium. As illustrated in the figure, separated grain boundaries were usually covered with pores the interval of which ranged from hundreds of nanometers to several microns. At the same time, many helium bubbles were found both in the matrix and at grain boundaries as shown in Fig. 2.

To obtain bubble size distribution data, specimens for transmission electron microscopy (TEM) were prepared from an adjacent region of a fractured portion. Observed results should thereby be very close to creep rupture. For every size distribution, measurements were run on at least three fields that were sampled from different grains so as to ensure statistical accuracy.

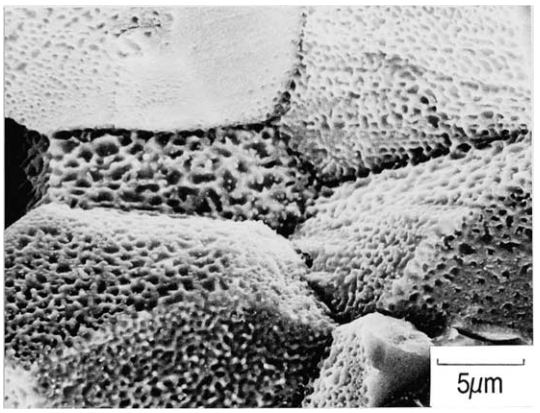

Fig. 1. Porous structure observed on intergranularly fractured facets of 'in-beam' ruptured DIN 1.4970 CW ($T = 873$ K, $C_{He} = 800$ appm, $\sigma = 420$ MPa, $t_r = 59$ ks).

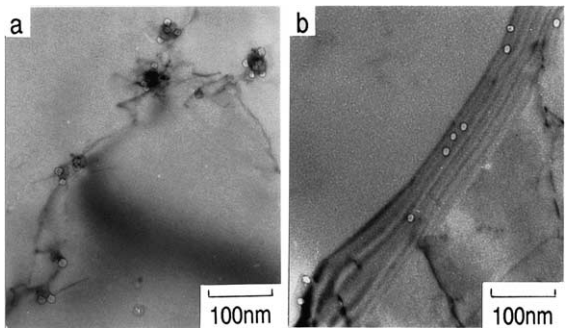

Fig. 2. Typical helium bubble microstructure in 82 series alloys after post-implantation creep rupture ($T = 923$ K, $C_{He} = 50$ appm, $\sigma = 120$ MPa): (a) in the matrix (alloy 8202), (b) at a grain boundary (alloy 8204).

3. Analysis and discussion

3.1. Embrittlement mechanism

The spongy-like structure shown in Fig. 1, which is prevalent in helium-embrittled materials, hints at the possibility of intergranular helium bubbles in fracture process. In order to examine this speculation, we assessed the minimum critical radius of intercrystalline bubbles in a manner described below and compared it with observed bubble size distributions.

The concept of the minimum critical radius, which was firstly introduced by Hyam and Sumner [6], signifies the size limit beyond which a bubble becomes energetically unstable and continues to grow infinitely to failure.

We have evaluated it through direct computation of the bubble growth rate by using following expression [7]:

$$\frac{\partial r}{\partial t} = \frac{Z_{\mathrm{v}}^{\mathrm{b}} D_{\mathrm{vB}} C_{\mathrm{vB}}^{\mathrm{e}}}{r} \exp\left(\frac{\Omega\sigma_N}{kT}\right) \times \left[1 - \exp\left\{\frac{\Omega}{kT}\left(\frac{2\gamma}{r} - P_{\mathrm{g}} - \sigma_N\right)\right\}\right], \quad (1)$$

where r is the bubble radius, $Z_{\mathrm{v}}^{\mathrm{b}}$ the bubble bias parameter for vacancies, D_{vB} the diffusion constant of vacancies, $C_{\mathrm{vB}}^{\mathrm{e}}$ the equilibrium vacancy concentration in grain boundary regions, Ω the atomic volume, σ_N the stress perpendicular to the boundary, γ the surface energy, P_{g} the gas pressure within the bubble and kT has its usual meaning. In calculating P_{g} we selected a hard sphere equation of state with Lennard-Jones potential [8], since bubble pressure treated here sometimes rises to very high values of several GPa.

Fig. 3 gives a result of above-mentioned computation in case of $\gamma = 2.0$ J/m^2. When stress is applied (during creep), $r_{\mathrm{c}}^* = 10.2$ nm is estimated as the minimum critical radius by the dotted curve in the figure. The growth rate-radius relationship is altered to the solid curve following the bold arrow after stress relief (creep rupture). The bubble therefore shrinks toward the newly introduced stable and equilibrium state of $r_{\mathrm{c}}^0 = 6.7$ nm by emitting vacancies. We use this 'relaxed' critical radius [9] for analyses described below, because TEM observations were made on stress-free samples.

Fig. 4 shows an example of intercrystalline bubble size distributions obtained under TEM, together with corresponding r_{c}^0. In this figure, bubbles larger than r_{c}^0 should indefinitely expand in an unstable manner by the mechanisms such as vacancy condensation and creep-constrained growth. The areal density and average distance of those over-critical bubbles are summarized in Table 2, along with the mean distance of dimples on the intergranularly ruptured faces, for all of the samples investigated. The both distances stay almost in the order of hundred nanometers and compare well with each other, provided that bubble coalescence occurred in some degree. This correspondence probably mirrors the grain boundary fracture triggered by the instability of helium bubbles.

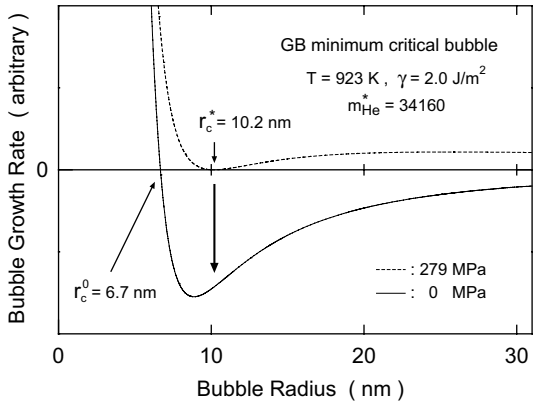

Fig. 3. Computed growth rate of a grain boundary helium bubble containing critical number of helium atoms (m_{He}^*) at $T = 923$ K, $\sigma = 279$ MPa, $\gamma = 2$ J/m^2 as a function of bubble radius.

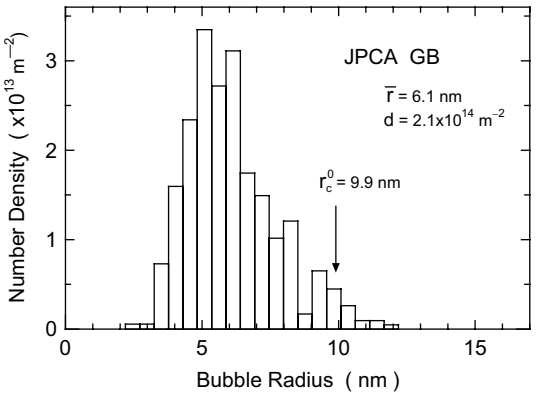

Fig. 4. Size distribution of intercrystalline helium bubbles in JPCA TMT after post-implantation creep rupture ($T = 923$ K, $C_{\mathrm{He}} = 50$ appm, $\sigma = 180$ MPa, $t_{\mathrm{r}} = 1.33$ Ms) with relaxed critical bubble radius (r_{c}^0).

3.2. Effect of helium retention in the matrix

It seems possible that helium embrittlement should be decreased by transcrystalline bubble entrapment. In this section, the amount of helium atoms both in the matrix and at the grain boundary will be assessed applying the bubble growth formula in the foregoing and the effect of intragranular helium confinement on suppression of the embrittlement will be quantitatively considered.

The number of helium atoms in a bubble of any given size can be numerically computed by equating $\partial r/\partial t$ in (1) to zero. Fig. 5 demonstrates this methodology and presents examples of the relation between stable bubble size and helium atom number inside. The calculations were done at $\sigma = 0$, since TEM investigations were performed in unstressed condition as previously noted. By adopting this method, we evaluated the number of helium atoms in individual bubbles like those in Fig. 2 both in the matrix and at grain boundaries, and thereby determined the fraction of helium atoms existing in grain interiors.

This fraction is plotted in Fig. 6 against the creep life ratio between helium bearing and free specimens, which is considered to be an appropriate parameter reflecting

Table 2
Microstructural data on critical bubbles at grain boundaries ($\gamma = 2$ J/m^2) and dimples on surfaces of intercrystalline fracture

Material	Creep parameter		GB helium bubble				GB dimple
	Stress (MPa)	Temperature (K)	m^*_{He}	r^0_c (nm)	d_c (m^{-2})	s_c (nm)	s_d (nm)
DIN 1.4970 CW	470	873	11 610	4.2	1.7×10^{12}	7.7×10^{2}	7.2×10^{2}
	440	873	13 410	4.5	8.7×10^{13}	1.1×10^{2}	–
	420	873	14 840	4.7	3.5×10^{13}	1.7×10^{2}	3.8×10^{2}
	400	873	16 500	4.9	5.1×10^{13}	1.4×10^{2}	4.3×10^{2}
AISI 316L CW	300	873	30 660	6.3	3.8×10^{13}	1.6×10^{2}	–
	240	873	49 340	7.7	5.9×10^{13}	1.3×10^{2}	3.9×10^{2}
JPCA SA	237	923	48 290	7.7	5.3×10^{13}	1.4×10^{2}	3.7×10^{2}
	207	923	64 250	8.7	4.5×10^{13}	1.5×10^{2}	2.3×10^{2}
	185	923	81 350	9.7	4.2×10^{13}	1.5×10^{2}	2.5×10^{2}
JPCA TMT	200	923	69 070	9.0	6.3×10^{13}	1.3×10^{2}	3.9×10^{2}
(coarse TiC)	191	923	76 080	9.4	4.2×10^{12}	4.9×10^{2}	4.6×10^{2}
	180	923	86 160	9.9	5.0×10^{12}	4.5×10^{2}	4.7×10^{2}
JPCA TMT	306	923	28 050	6.1	3.0×10^{13}	1.8×10^{2}	4.1×10^{2}
(fine TiC)	293	923	30 770	6.4	2.2×10^{13}	2.1×10^{2}	4.1×10^{2}
	279	923	34 160	6.7	1.5×10^{13}	2.6×10^{2}	4.1×10^{2}
8201 TMT	120	923	200 350	14.4	1.0×10^{12}	9.9×10^{2}	1.0×10^{3}
8202 TMT	120	923	200 350	14.4	4.3×10^{12}	4.8×10^{2}	1.1×10^{3}
8203 TMT	120	923	200 350	14.4	2.0×10^{13}	2.2×10^{2}	1.1×10^{3}
8204 TMT	120	923	200 350	14.4	–	–	1.3×10^{3}
8206 TMT	120	923	200 350	14.4	2.0×10^{12}	7.1×10^{2}	9.0×10^{2}
8207 TMT	120	923	200 350	14.4	4.6×10^{12}	4.7×10^{2}	8.1×10^{2}

m^*_{He}: critical number of helium atoms, r^0_c: minimum critical bubble radius after stress relaxation ($\sigma = 0$), d_c: areal number density of super-critical bubbles, s_c: mean spacing of super-critical bubbles, s_d: average distance of dimples on GB fractured surface.

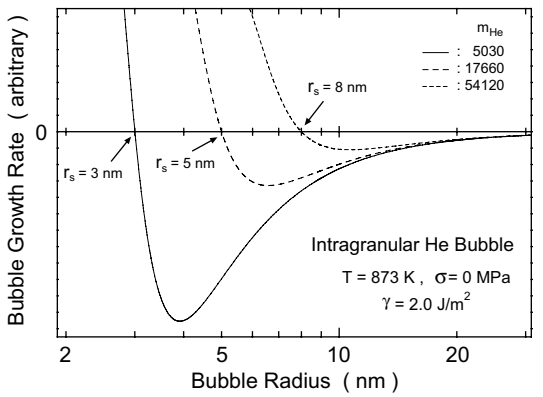

Fig. 5. Radius dependence of bubble growth rate at $T = 873$ K, $\sigma = 0$ MPa, $\gamma = 2$ J/m^2 showing relation between equilibrium bubble size (r_s) and helium atom (m_{He}) in its interior.

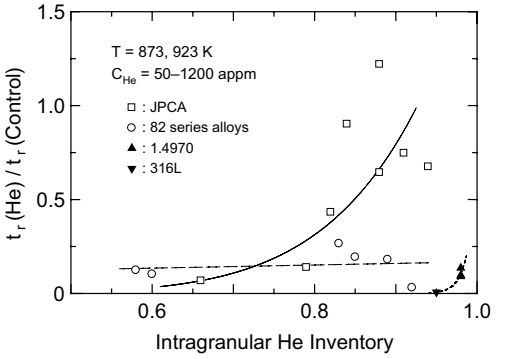

Fig. 6. Creep life ratio of helium injected specimens to uninjected controls versus intragranular helium inventory plot for creep-tested Fe–Ni–Cr austenitic materials.

the degree of helium embrittlement in case of our creep tests [5]. Although an increasing tendency of creep rupture time ratio with increasing capability of transgranular helium capture was observed for each alloy, the former remained at very low values in some alloys even if the high level of helium detention in the matrix over 90% was attained. This reveals a limit of transgranular helium entrapment in preventing helium embrittlement.

4. Conclusion

Bubble microstructures of helium-implanted and creep ruptured Fe–Ni–Cr alloys were theoretically ana-

lyzed considering energetical bubble stability over the wide ranges of experimental parameters documented in Table 1. The main conclusions are as follows.

(1) Unstable growth of grain boundary bubbles larger than the minimum critical size seems to operate as a principal mechanism of helium embrittlement.
(2) Helium bubble capturing in grain interiors would contribute to suppression of helium embrittlement to a certain extent, but not enough to eliminate it.

Acknowledgements

A part of this study was financially supported by the Budget for Nuclear Research of the Ministry of Education, Culture, Sports, Science and Technology, based on the screening and counseling by the Atomic Energy Commission.

References

[1] H. Ullmaier, Nucl. Fusion 24 (1984) 1039.
[2] L.K. Mansur, M.L. Grossbeck, J. Nucl. Mater. 155–157 (1988) 130.
[3] N. Yamamoto, H. Schroeder, J. Nucl. Mater. 155–157 (1988) 1043.
[4] N. Yamamoto, H. Shiraishi, H. Kamitsubo, I. Kohno, T. Shikata, A. Hishinuma, J. Nucl. Mater. 133&134 (1985) 493.
[5] N. Yamamoto, J. Nagakawa, H. Shiraishi, J. Nucl. Mater. 226 (1995) 185.
[6] E.D. Hyam, G. Sumner, Proceedings of the International Symposium on Radiation Damage in Solids, vol. 1, IAEA, Vienna, 1962, p. 323.
[7] R. Bullough, S.M. Murphy, J. Nucl. Mater. 133&134 (1985) 92.
[8] I.R. Brearley, D.A. MacInnes, J. Nucl. Mater. 95 (1980) 239.
[9] H. Trinkaus, H. Ullmaier, J. Nucl. Mater. 155–157 (1988) 148.